Applied Catalysis B: Environmental 168-169 (2015) 68–76

Contents lists available at ScienceDirect

Applied Catalysis B: Environmental

journal homepage: www.elsevier.com/locate/apcatb

Catalytic reduction of NO with H_2 over redox-cycling Fe on CeO_2

Dario Prieto-Centurion[a,1], Todd R. Eaton[a], Charles A. Roberts[b], Paul T. Fanson[b], Justin M. Notestein[a,*]

[a] Department of Chemical and Biological Engineering, Northwestern University, 2145 Sheridan Road, Evanston, IL 60208, USA
[b] Toyota Motor Engineering & Manufacturing North America, Inc., 1555 Woodridge Avenue, Ann Arbor, MI 48105, USA

ARTICLE INFO

Article history:
Received 22 August 2014
Received in revised form
19 November 2014
Accepted 27 November 2014
Available online 18 December 2014

Keywords:
deNO$_x$
Ceria
Redox
Emissions
XANES

ABSTRACT

Removal of NO_x species from automotive emissions continues to be a challenge, particularly using replacements for Pt-group metals. Here, we demonstrate the synthesis of FeO_x domains on CeO_2 from the precursor Fe ethylenediaminetetraacetate (NaFeEDTA) and its utility in the reduction of NO with H_2 as a model reaction for tailpipe emissions. Diffuse-reflectance UV–visible and X-ray absorption near-edge spectroscopies indicate the formation of small, non-crystalline FeO_x domains. Using the EDTA precursor, TPR and in situ XANES show that up to 45% of the FeO_x centers were capable of undergoing redox cycles in H_2 up to 550 °C, whereas only 23% of FeO_x centers derived from $Fe(NO_3)_3$ were redox active. Similarly, at comparable Fe surface densities, the FeEDTA-derived catalysts were more active than the nitrate-derived materials in the reduction of NO to N_2 (85–95% selectivity) with H_2 at 450 °C. The presence of both the bulky organic ligand and the alkali is essential for the observed enhancements in fraction redox active and to achieve high NO reduction rates. Rates over all materials were fit to a single correlation against the number of redox-active FeO_x centers, suggesting that these are the catalytic active sites. The new materials describe here may offer new avenues for emissions control without Pt-group metals or substituted zeolites.

© 2014 Elsevier B.V. All rights reserved.

1. Introduction

The removal of NO_x from automotive emissions continues to be an important challenge in heterogeneous catalysis. The current industry standard, the three-way catalyst, is a remarkable achievement in emissions control, but relies on scarce and costly noble metals such as Pd, Pt and Rh [1], hence an interest in catalysis by earth-abundant species. Metal exchanged zeolites have garnered academic and industrial interest as potential replacements due to their low cost and high activity in the removal of NO [2–12]. Much focus has been placed on Fe-exchanged ZSM-5 zeolite, in particular, due to its activity in NO reduction with NH_3 [4–7] and hydrocarbons [7–10] and high selectivity toward N_2 [7,9]. One concern is durability in the presence of H_2O [10], which depends strongly on the framework. It is generally accepted that low nuclearity species are responsible for the catalytic behavior of Fe-exchanged zeolites. Isolated Fe ions [7,8,13], μ-oxo dimers [10,11,14], and oligomeric species [9] are potential active sites proposed in the literature.

Several studies have attempted to reproduce the active structures and reactivity of Fe-exchanged zeolites on more common oxide supports. Incipient wetness impregnation (IWI) of oxide supports with $Fe(NO_3)_3$ solutions – ideal due to its simplicity and scalability – produces a multitude of Fe structures on CeO_2 [15,16], ZrO_2 [16,17], and SiO_2 [16–19] even at fractions of monolayer coverage. Adsorption–precipitation of $FeSO_4$ produces a narrower distribution of surface species on SiO_2, but still is comparable to IWI of $Fe(NO_3)_3$ [20,21]. Overall, structurally heterogeneous surfaces obscure the underlying chemistry and make difficult the development of fundamental insights. Advanced techniques involving chemical vapor deposition of $FeCl_3$ [22] or grafting of Fe siloxide precursors [23,24] are more selective in producing dimers and monomers, but may be difficult to scale up.

Furthermore, similar FeO_x structures on zeolitic and non-zeolitic supports need not display the same catalytic behavior. For example, supports like CeO_2 undergo redox cycles, store oxygen, and chemisorb H_2 [25,26], all of which can influence the behavior of the surface FeO_x species. Hence, the development of support-specific synthesis–structure–reactivity relations is a necessity, particularly on reducible supports.

Here, we demonstrate a route to FeO_x surfaces species of controlled dispersion on CeO_2 based on prior work by some of the authors for the synthesis of FeO_x–SiO_2 [27,28]. Here, catalysts are

* Corresponding author. Tel.: +1 847 491 5357; fax: +1 847 491 3728.
E-mail address: j-notestein@northwestern.edu (J.M. Notestein).
[1] Current address: SABIC Americas, Houston, TX 77042, USA.

http://dx.doi.org/10.1016/j.apcatb.2014.11.055
0926-3373/© 2014 Elsevier B.V. All rights reserved.

prepared by IWI of aqueous, anionic Fe^{3+} complexes of ethylenediaminetetraacetic acid (EDTA) onto CeO_2 supports, followed by oxidative thermal removal of the ligand. This work explores the changes in FeO_x structure, redox behavior, and reactivity in NO reduction with H_2, which accompany changes in synthesis precursor ($FeEDTA^-$ or $Fe(NO_3)_3$), alkali dopant, and surface density, all at sub-monolayer coverage. Although H_2 is not a reductant present in automotive emissions, this model system allows clearer insights into critical NO activation steps.

2. Experimental

2.1. Materials and instruments

All reagents are obtained from Sigma–Aldrich and used as received. Catalyst precursors are synthesized under air at ambient conditions. Non-porous CeO_2 support (C.I. Kasei Co., Ltd., NanoTek powder) is dried at 120 °C under ambient air and pressure for >12 h before use.

N_2 physisorption isotherms are obtained using a Micromeritics ASAP 2010 instrument. Specific surface areas were extracted from N_2 physisorption isotherms using the BET equation [29]. Before measurements, all materials are degassed 6 h at <5 mTorr and 120 °C to release absorbed water.

Elemental analysis is performed using a Varian MPX ICP-OES instrument. Samples are prepared by dissolving 50 mg of solids in 1 mL of HF and subsequently diluting to 50 mL with H_2O. Metal contents are quantified by comparison against standards of known concentration. Diffuse reflectance UV–visible (DRUV–vis) spectra are collected using a Shimadzu 3600 UV–visible–NIR spectrometer with a Harrick Praying Mantis diffuse reflection attachment. Polytetrafluoroethylene (PTFE) is used as the baseline standard and diluent. All materials are mixed with five mass equivalents of PTFE and thoroughly ground with mortar and pestle before analysis. The resulting diffuse reflectance spectra are converted to pseudo-absorption using the Kubelka–Munk transform [30]. Solution UV–vis spectra are acquired with a Shimadzu 3600 UV–visible–NIR spectrometer using a standard 1 cm pathlength quartz cell. Thermogravimetric analyses (TGA) are performed using a TA Instruments Q500 thermogravimetric analyzer fitted with an evolved gas analysis furnace. For combustion analysis, materials are heated in 100 sccm 90% O_2 and 10% He with a temperature program of 10 °C min^{-1} to 800 °C.

2.2. NaFeEDTA and NH_4FeEDTA synthesis

The preparation of sodium Fe(III) ethylenediaminetetraacetate (NaFeEDTA) and ammonium Fe(III) ethylenediaminetetraacetate (NH_4FeEDTA) is based on that by Meier and Heinemann [31]. H_4EDTA (10 mmol) and $Fe(NO_3)_3{\cdot}9H_2O$ (10 mmol) are mixed with 25 mL of H_2O (>18 mΩ) in a 100 mL two-neck round-bottom flask. The mixture is then heated to 60 °C under ambient air while stirring until a solution forms.

To form NaFeEDTA, four equivalents of $NaHCO_3$ (40 mmol) are slowly added to fully deprotonate the H_4EDTA ligand, and the desired product precipitates out of solution upon cooling to ambient temperature. The resulting yellow solid is separated by filtration, washed with 5 mL of H_2O at 0 °C to remove $NaNO_3$ impurities, and with 15 mL of acetone to remove excess H_2O. Finally, the yellow solid is dried under dynamic vacuum (20 mTorr) for 12 h. TGA of the dry material between 150 °C and 550 °C showed a mass loss due to combustion corresponding to 98% purity according to the ratio of organic to inorganic components.

To form NH_4FeEDTA, four equivalents of NH_4HCO_3 (40 mmol) are used to deprotonate the H_4EDTA ligand. The solution is reduced to ~5 mL by rotary evaporation and stored at −20 °C overnight. The resulting crystals are separated by filtration, washed with acetone, and dried under dynamic vacuum (20 mTorr) for 12 h. TGA of the dry material between 200 °C and 550 °C showed a mass loss due to combustion corresponding to 99.3% purity according to the ratio of organic to inorganic components.

Table 1
Characteristics of FeO_x–CeO_2 materials.

Material #	Precursor	Support	Fe loading[a]			Notes
			wt%	μmol g^{-1}	at. nm^{-2}	
1	NaFeEDTA	CeO_2	0.18	32	0.19	*r*
2	NaFeEDTA	CeO_2	0.34	60	0.36	
3	NaFeEDTA	CeO_2	0.52	92	0.55	
4	NaFeEDTA	CeO_2	0.53	94	0.56	*r*, *x*
5	NaFeEDTA	CeO_2	0.81	145	0.87	*r*, *x*
6	NaFeEDTA	CeO_2	1.16	207	1.23	*r*
7	NaFeEDTA	CeO_2	1.38	246	1.47	*r*, *x*
8	NH_4FeEDTA	CeO_2	0.48	86	0.51	
9	NH_4FeEDTA	Na/CeO_2	0.49	87	0.52	
10	$Fe(NO_3)_3$	Na/CeO_2	0.43	82	0.49	*r*
11	$Fe(NO_3)_3$	Na/CeO_2	0.87	164	0.98	*r*, *x*
12	$Fe(NO_3)_3$	Na/CeO_2	1.35	255	1.52	*r*

[a] Loadings confirmed by ICP-OES and surface densities based on BET surface area of the neat support.
r – material underwent multiple cycles of TPR.
x – XANES spectra in Fig. 6.

2.3. Support modification

The support, non-porous CeO_2 (C.I. Kasei Co., Ltd. NanoTek powder) with surface area of 101 m^2 g^{-1}, is modified by incipient wetness impregnation (IWI) with aqueous solutions of $NaHCO_3$ (0.1–0.6 M). The incipient wetness volume required to wet the support is approximated by the total uptake volume determined by N_2 physisorption of neat CeO_2. Following impregnation, the supports are dried in partially covered containers under ambient conditions for 24 h and then heated to 120 °C for 12 h to create Na/CeO_2. TGA of the dry materials show no evidence of residual carbonates, combustible materials, or volatile groups on the surface. N_2 physisorption of the dry materials showed changes in surface area lower than 10% and a decrease in uptake volume of ~30% (Supporting Information Table S1).

2.4. Catalyst preparation

Iron is deposited on neat and alkali-modified CeO_2 by IWI with aqueous solutions of NaFeEDTA (0.1–0.3 M), NH_4FeEDTA (0.1–0.2 M), and $Fe(NO_3)_3$ (0.2–0.6 M). In all cases where Na is present in the final catalyst, Fe and Na are present in equimolar amounts. No evidence of dimeric FeEDTA complexes – with a characteristic UV–visible peak at 475 nm – is observed in the impregnation solutions [32]. Following impregnation, materials are dried for 24 h in partially covered containers under ambient conditions and for 12 h under dynamic vacuum (~20 mTorr). The aqueous solubility of NaFeEDTA (~0.3 M) limits single impregnations on CeO_2 (surface area = 101 m^2 g^{-1}, incipient wetness volume = 275 μL g^{-1}) to a maximum loading of approximately 0.6 Fe nm^{-2}. To surpass this limit, the impregnation and drying cycle is repeated multiple times.

The dry materials undergo oxidative heat treatment under static ambient air from room temperature to 550 °C at a ramp rate of 10 °C min^{-1} after which point they are generically referred to as FeO_x–Na/CeO_2. Fe surface densities vary in the range 0.2–1.5 Fe nm^{-2} (Table 1), as calculated from ligand combustion by TGA and confirmed by digestion and ICP-AES.

2.5. Temperature-programmed reduction

Temperature-programmed reduction (TPR) experiments are performed in a TA Instruments Q500 TGA fitted with a Pfeiffer Thermostar Q200 process mass spectrometer. As-prepared materials are pretreated in 100 sccm 90% O_2 and 10% He following a temperature program of 10 °C min^{-1} to 550 °C and subsequent 15 min temperature hold. The pretreated materials are cooled to ambient temperature in 100 sccm He, then heated again at 10 °C min^{-1} to 550 °C in 100 sccm 4.5% H_2, 4.5% Ar, balance He. The evolved H_2O signal, $m/z = 18$, is normalized by the constant flow of Ar, $m/z = 40$, and calibrated against the reduction of known amounts of CuO to metallic Cu under the same conditions.

Selected samples (marked *r* in Table 1) were subjected to a second oxidation and reduction cycle. After the first TPR experiment, samples are cooled to near ambient temperature in 100 sccm He, before undergoing the next cycle of oxidation, cooling under inert, and reduction.

2.6. In situ X-ray absorption spectroscopy during H_2-TPR

X-ray absorption near-edge structure (XANES) analysis was performed at the bending magnet D beamline of the Dupont–Northwestern–Dow Collaborative Access Team (DND-CAT), in Sector 5 of the Advanced Photon Source at Argonne National Laboratory. Incident and transmitted intensities were measured with Canberra ionization chambers. Beam energies were calibrated against Fe metal foil measured in transmittance and its K-edge was set to 7112 eV. FeO and Fe_2O_3 standards were brushed on Capton tape and their spectra were also measured in transmittance.

Supported Fe materials were pressed into 50 mg pellets 2.5 cm in diameter. Single pellets were mounted on a stainless steel heated cell designed for transversal gas flow and sealed with a Be back window and Capton front window. To ensure pellets remained against the front Capton sheet, the space between windows was filled with a loose bed of quartz wool. Due to the low Fe content of the pellets, spectra were measured as fluorescence intensity using a four-channel SII Vortex-ME4 detector. Samples were mounted at incident angle $\theta = 45°$ with respect to the beam and detector, which were perpendicular to one another. Before starting the temperature program, spectra of the pellets loaded in the sample holder were compared to those of the corresponding powder materials brushed on Capton tape and measured also as fluorescence intensity.

Once mounted, pellets were subjected to transversal flow of 50 sccm 3.5% H_2 and balance He. The heated flow cell was held at ambient temperature, 150 °C, 250 °C, 340 °C, and 430 °C for 2 h each while spectra were collected. Between holds, the temperature was ramped at ~10 °C min^{-1}. Note that these are true sample temperatures.

2.7. Catalytic reactions

NO reduction by H_2 was performed at atmospheric pressure in a quartz U-tube reactor (OD ¼″, ID 1/8″). Beds composed of 25 mg of catalyst diluted in 0.50 g of non-porous quartz sand were packed in down flow between plugs of quartz wool. Before mixing, the catalyst was pressed into pellets, lightly crushed, and sieved to 40–100 mesh size – similar to the quartz diluent. A thermocouple placed against the top of the catalyst bed was used to monitor and record temperature, which was controlled using a J-KEM 4700 safety temperature controller connected to a Applied Test Systems upright tube furnace (ID 2.5″). The thermocouple and quartz diluents showed no catalytic activity in control experiments.

The reactor inlet was connected to a gas manifold delivering 50 sccm (standard cm^3 per minute) of 3.3% NO, 3.3% H_2, 3.3% Ar, and balance He, corresponding to a gas hourly space velocity of approximately 10^4 h^{-1} for the total loading of catalyst and diluent given above. The outlet was connected to a Pfeiffer Thermostar Q200 process mass selective detector measuring reactant and product concentrations. The MSD signal corresponding to Ar ($m/z = 40$) was used as an internal standard by which all other signals were normalized. MSD signals corresponding to NO ($m/z = 30$) and N_2 ($m/z = 28$) were calibrated against 50 sccm flows with concentrations of NO and N_2 between 1% and 5%, which were prepared by dilution of 5% NO/He and 5% N_2/He mixtures in pure He. To avoid signal crossover with H_2O, $m/z = 16$ was used to track NH_3 evolution. This signal was calibrated against the thermal decomposition at 42 °C of known amounts of NH_4HCO_3 in a 50 sccm flow of He.

Packed reactors were fed 50 sccm of the reaction mixtures, heated at 10 °C min^{-1} to 150 °C, 250 °C, 350 °C, 450 °C, and 550 °C, and held at each temperature for 1 h. Complete disappearance of signals corresponding to atmospheric N_2, O_2, H_2O, and CO_2, as well as surface H_2O, was observed within 20 min at 150 °C. Additionally, because no reaction was observed at 150 °C, the gas concentrations of the final 30 min at this temperature were used as the baseline.

3. Results and discussion

3.1. Diffuse reflectance UV–visible spectrophotometry

For both synthesis methods, powder X-ray diffraction (XRD) shows no indication of crystalline FeO_x phases. Because even the highest surface loading is only a fraction of a statistical monolayer, typically assumed to form at 4–6 atoms nm^{-2}, the formation of crystallites would not be expected. Thus, diffuse reflectance UV–visible (DRUV–vis) spectrophotometry was used to examine the dispersion of Fe surface species on the FeO_x–Na/CeO_2 materials. For inert oxide supports, isolated Fe^{3+} ions are expected to show oxygen-to-metal charge transfer bands below 300 nm, two-dimensional oligomers between 300 nm and 500 nm, and larger aggregates above 500 nm [15,18,24,33,34]. For the materials in this study, bands that could correspond to isolated ions are obscured by the strong absorption of CeO_2 below 350 nm. For redox active supports such as CeO_2, red-shifted absorption bands could also correspond, in principle, to metal-to-metal charge transfer between Fe and Ce.

Fig. 1 shows FeO_x–Na/CeO_2 prepared from NaFeEDTA and $Fe(NO_3)_3$. Both sets of materials show absorption tails extending beyond that of CeO_2 and growing with increasing Fe loading. Supporting Information Fig. S1 shows a corresponding increase in red color with increasing loading. For all materials, pseudo-absorption intensity beyond that of CeO_2 is predominantly in the range of 300–500 nm, suggesting a significant population of two-dimensional oligomers or small clusters. At the highest loadings of the EDTA-derived materials, an additional feature appears at higher wavelengths, likely associated with larger, but still non-crystalline oxide clusters. For a given loading, there are no significant differences in color between samples made by the two methods (Supporting Information Fig. S1). Studies by others have observed that supports with surface vacancies such as CeO_2 tend to incorporate Fe^{3+} and other cations into vacant sites [16,35]. Therefore, the negative charge and large size of the FeEDTA complex may alter the distribution of how the Fe^{3+} ions interact with the surface vacancies and reducible sites on CeO_2, as compared to $Fe(NO_3)_3$. This distribution is quantified by examining their reducibility below.

3.2. Temperature-programmed reduction

Dispersion and agglomeration of supported transition metal oxides are related to redox properties which can be probed by

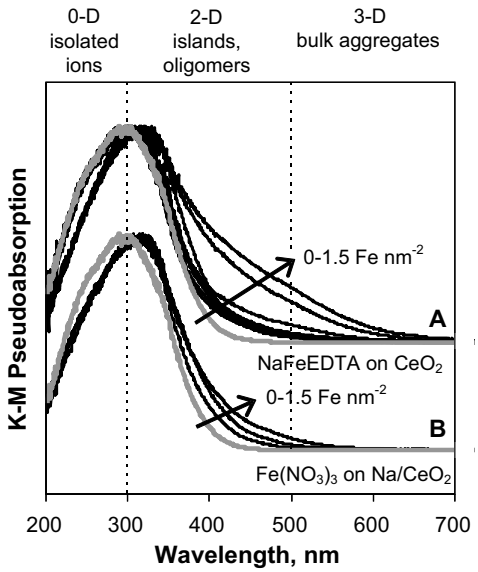

Fig. 1. DRUV–vis spectra of FeO_x–Na/CeO_2 prepared from (A) NaFeEDTA on CeO_2 and (B) $Fe(NO_3)_3$ on Na/CeO_2. The gray line corresponds to Na-doped CeO_2 with a surface loading of 1.0 Na nm^{-2}.

TPR. Monomeric Fe^{3+} structures interacting strongly with inert oxide supports are expected to reduce at higher temperature than agglomerates more closely resembling bulk oxides [18]. Specifically, isolated Fe^{3+} ions on an irreducible support like SiO_2 are expected to reduce in H_2 between 600 °C and 700 °C [27,28], while 2D sheets or clusters and 3D aggregates reduce around 500 °C and 400 °C, respectively [21,34]. These generalizations do not necessarily hold on redox-active or zeolite supports. Regardless of their assignment, the highest temperature reduction features are not accessible here due to bulk reduction of CeO_2 starting at ~600 °C. Such sites are also not relevant to the catalytic reactions described here, which occur at 550 °C and below.

3.3. General behavior

Fig. 2A shows the TPR profiles of FeO_x–Na/CeO_2 prepared from NaFeEDTA on CeO_2 and that of Na/CeO_2. The total H_2O evolved from these materials during reduction between 150 and 550 °C (Fig. 3) increases linearly with Fe loading. The non-zero intercept matches the H_2O evolved during the reduction of neat CeO_2 in the same temperature range. While both CeO_2 and FeO_x reduce in this temperature range, the excess evolved H_2O – that of FeO_x–Na/CeO_2 less that of Na/CeO_2 – is directly proportional to the Fe content. This proportionality shows that the fractional reduction is independent of surface density within this range of loadings. The slope of the linear fit in Fig. 3, 0.23 mol excess H_2O per mol Fe, corresponds to an average reduction from Fe(III) to Fe(II) of 45 ± 6%. Keep in mind that the parallel reduction of the CeO_2 surface is also occurring, but not factored into these values. As a corollary, approximately half the total Fe is likely present as highly dispersed surface or near-surface Fe species that do not undergo redox transitions within the explored temperature range.

Materials prepared from $Fe(NO_3)_3$ show similar TPR profiles as those derived from FeEDTA (Fig. 2B), except that the excess H_2O evolved during reduction (Fig. 3) corresponds to an average reduction from Fe(III) to Fe(II) of 23 ± 6%. The lower extent of reduction relative to materials prepared from FeEDTA indicates that the nitrate precursor results in different interactions with the ceria support, which creates sites unreducible in this temperature range. This is in agreement with our hypothesis that both precursors yield oligomers and small clusters of FeO_x, but differently distribute Fe^{3+} ions amongst vacancies, reducible sites, and other regions on the CeO_2 surface, with EDTA increasing the number of reducible sites.

3.4. Fe speciation

TPR profiles can be deconvoluted into four Gaussian curves here ascribed to separate reduction events (example in Fig. 2C and D). It is clear from TPR profiles of Na/CeO_2 (Fig. 2A and B, gray lines) that reduction events centered on 350 °C and 500 °C correspond to the surface reduction of the support, in agreement with observations reported in the literature [15]. Thus, the ceria surface is reducing in parallel with the reduction of the FeO_x sites.

Materials prepared from FeEDTA display two additional features; one at 400 °C present in all materials and another at 300 °C which emerges at loadings above 0.9 Fe nm^{-2} (Fig. 2C). The low reduction temperatures and the lack of crystalline FeO_x are consistent with these features being assigned as different types of two-dimensional FeO_x oligomers or small clusters well dispersed on the surface. Materials prepared from $Fe(NO_3)_3$ show the reduction event at 400 °C only (Fig. 2D), assigned as a single type of FeO_x cluster, again to be consistent with the DRUV–vis. The remaining FeO_x (~55% for EDTA-derived materials and ~75% for nitrate-derived materials) may be present as several different types of non-crystalline FeO_x that are not reducible over this temperature range.

3.5. Fe^{3+}–Fe^{2+} redox cycle

As described in the experimental section, selected materials (marked *r* in Table 1) underwent a second oxidation to 550 °C and TPR after the first TPR experiment. The total area of the reduction features at 350 °C and 500 °C corresponding to CeO_2 is unaffected, indicating the support reduces to the same extent during the second cycle. However, at the highest Na loadings, the CeO_2 reduction feature at 350 °C broadens out on a second reduction cycle without a change in total integrated area (Supporting Information Fig. S2). The phenomenon is attributed to the higher alkali loading combined with the repeated heating cycles. The small drop in surface area at higher Na loadings (Supporting Information Table S1) also suggests structural alterations of the support as consequence of the alkali and repeated temperature cycling.

Materials with loadings of 0.9 Fe nm^{-2} or below display only one feature correlated to FeO_x (centered at 400 °C) which changes minimally between cycles (Supporting Information Fig. S3), indicating these species are capable of reversible Fe^{3+}–Fe^{2+} redox cycles relevant for catalysis. For materials prepared with FeEDTA and loadings of 1.2 and 1.5 Fe nm^{-2} such as shown in Fig. 2C, the unique feature at 300 °C is absent on the second TPR (Supporting Information Fig. S3), and the reduction event near 400 °C appears at slightly lower temperature and decreases substantially in total area (by 24% and 42% for 1.2 and 1.5 Fe nm^{-2}, respectively) in the second TPR. The net result is that the fraction of Fe atoms undergoing reversible Fe^{3+}–Fe^{2+} redox cycles decreases beyond ~0.9 Fe nm^{-2} (data summarized in Fig. 4). Interestingly, there is no accompanying significant change in the DRUV–vis spectra after multiple TPR cycles. Thus, we ascribe the change in reducibility to small changes in the distribution of FeO_x sites and how they interact with the CeO_2 surface, rather than wholesale changes to the FeO_x aggregates themselves. The particular reducibility limit of ~0.9 nm^{-2} may suggest an intrinsic feature related the reducible surface sites on this ceria support. A third oxidation–reduction cycle of the materials with 1.2 Fe nm^{-2} (Supporting Information Fig. S4) shows the

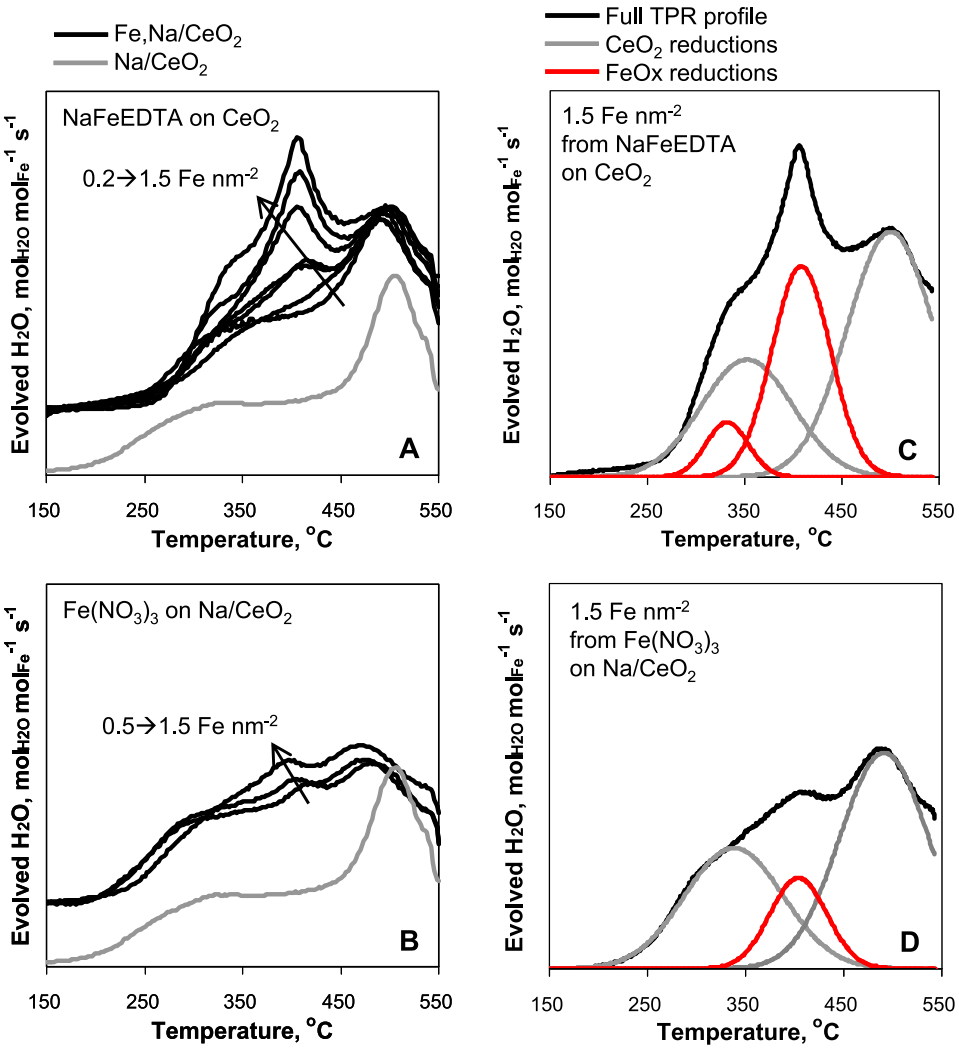

Fig. 2. Temperature-programmed reduction profiles for FeO_x–Na/CeO_2 prepared from (A) NaFeEDTA on CeO_2 and (B) $Fe(NO_3)_3$ on Na/CeO_2 at 0–1.5 Fe nm^{-2}. (C) 1st TPR of 1.5 Fe nm^{-2} via NaFeEDTA on CeO_2 deconvoluted into four Gaussian curves, here ascribed to CeO_2 surface reduction (350 °C and 500 °C) and FeO_x domains (400 °C and 300 °C). The 400 °C is present in all materials and increases with loading. The feature at 300 °C is only present above 0.9 Fe nm^{-2} and for the first reduction cycle (D) TPR for 1.5 Fe nm^{-2} via $Fe(NO_3)_3$ on Na/CeO_2 deconvoluted into three features, which are stable with multiple redox cycles.

same profile as the second TPR, indicating that the surface species stabilize after the first redox cycle.

3.6. X-ray absorption spectroscopy

Fig. 5 shows pre-edge and XANES spectra of FeO_x–Na/CeO_2 materials during reduction with dilute H_2 between ambient temperature and 430 °C. The spectra correspond to materials (marked *x* in Table 1) prepared from NaFeEDTA on CeO_2 (Fig. 6A–C) and $Fe(NO_3)_3$ on Na-modified CeO_2 (Fig. 5D). All the materials tested show pre-edge features more intense than those of the bulk oxide standards, indicating undercoordinated FeO_x species [36]. For materials derived from NaFeEDTA on CeO_2 (Fig. 5A–C), the intensity of the pre-edge band decreases with increasing Fe surface density, which is consistent with the shift in DRUV–vis spectra, and suggesting increasing Fe–O coordination numbers with increasing loading, which could indicate larger clusters or more thorough incorporation into the ceria lattice.

For all materials, the absorption edge remains between that of Fe^{3+} and Fe^{2+} at all temperatures. This indicates the presence of the Fe^{2+} oxidation states even after the original calcination and a return to ambient temperature. To determine the relative concentration of the two oxidation states, the spectra of the supported materials

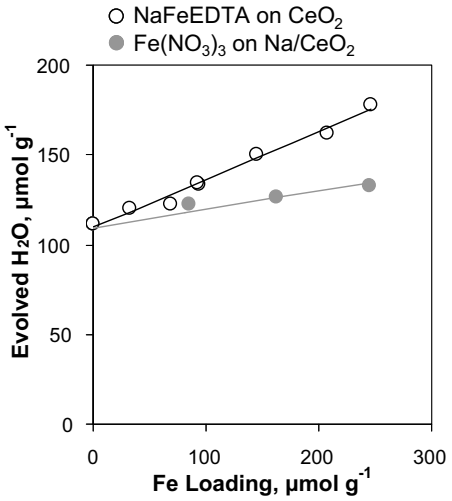

Fig. 3. Total H_2O evolved by FeO_x–Na/CeO_2 materials during TPR from ambient temperature to 550 °C. The *y*-axis intercept corresponds to the H_2O evolved from surface reduction of CeO_2.

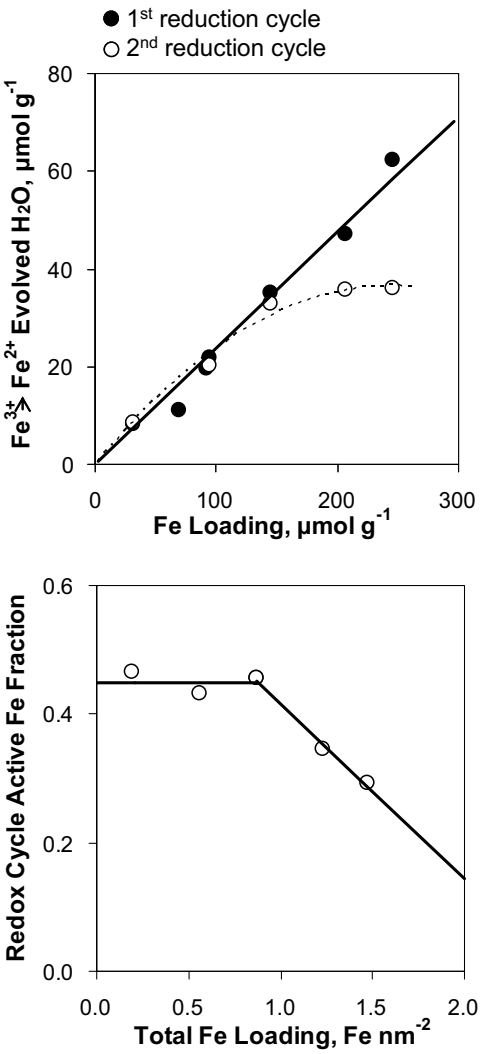

Fig. 4. (Top) Evolved H_2O in excess of that evolved by CeO_2 alone, which corresponds to the reducible Fe species, plotted against total Fe. Sample is FeO_x–Na/CeO_2 from NaFeEDTA. (Bottom) The fraction of Fe capable of undergoing reversible Fe^{3+}–Fe^{2+} redox cycles for FeO_x–Na/CeO_2 prepared from NaFeEDTA begins to decrease above 1.0 Fe nm^{-2}.

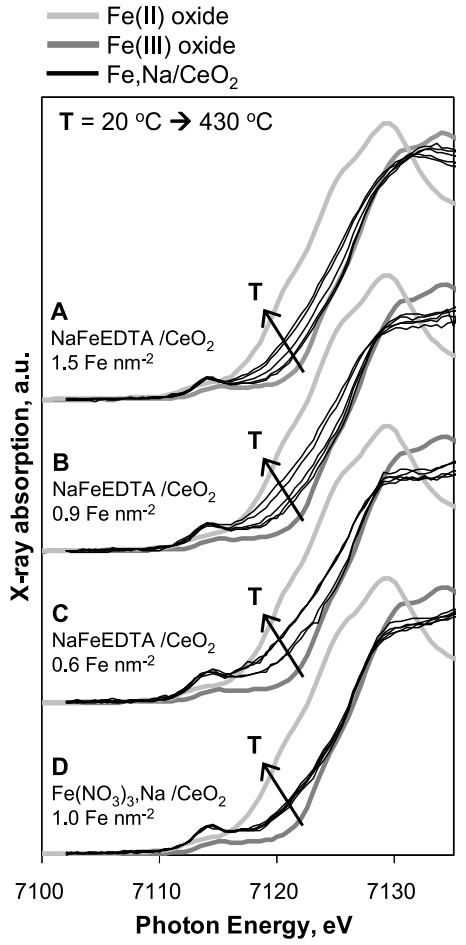

Fig. 5. Pre-edge and XANES spectra collected during reduction in H_2 flow from ambient temperature to 430 °C for FeO_x–Na/CeO_2 from (A) NaFeEDTA at 1.5 Fe nm^{-2}, (B) NaFeEDTA at 0.9 Fe nm^{-2}, (C) NaFeEDTA at 0.6 Fe nm^{-2}, and (D) $Fe(NO_3)_3$ at 1.0 Fe nm^{-2}. Reference spectra of Fe_2O_3 and FeO are given in gray.

are fitted to linear interpolations of those of bulk FeO and Fe_2O_3 in the near-edge region between 7117 eV and 7124 eV – the range where the absorption edges of Fe^{2+} and Fe^{3+} appear. This method reliably predicts the fractions of Fe^{3+} and Fe^{2+} in experimentally acquired spectra of mixed valence bulk Fe_3O_4. In addition, samples of calcined FeO_x on SiO_2 made by the same methods show 100% Fe^{3+} oxidation state, as expected.

For materials prepared from NaFeEDTA on CeO_2, the change in absorption edge between ambient temperature and 430 °C corresponds to 28%, 39%, and 37% reduction from Fe^{3+} to Fe^{2+} for Fe loadings 0.6 Fe nm^{-2}, 0.9 Fe nm^{-2}, and 1.5 Fe nm^{-2}. According to TPR experiments, average Fe^{3+} to Fe^{2+} reduction up to 430 °C yields partial Fe^{3+} to Fe^{2+} reductions of 32%, 37%, and 39%, respectively; the two experiments are in remarkable agreement. For the material prepared from $Fe(NO_3)_3$ on Na/CeO_2, the change in absorption edge between ambient temperature and 430 °C corresponds to approximately 9% of the Fe transition from Fe^{3+} to Fe^{2+}, while TPR experiments show a slightly higher value of 17% reduction of the FeO_x in this material up to 430 °C. Given the lower extent of reduction, the values remain in good agreement.

Overall, X-ray absorption and TPR experiments are in good quantitative and qualitative agreement, and both indicate that

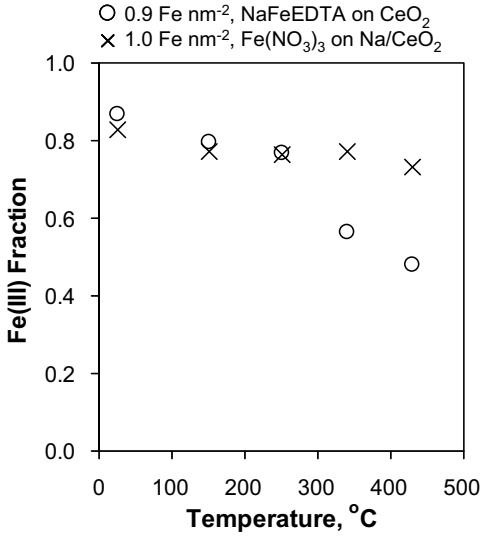

Fig. 6. Fraction of Fe^{3+} present as a function of temperature for 0.9 and 1.0 Fe nm^{-2} materials prepared from NaFeEDTA on CeO_2 and $Fe(NO_3)_3$ on Na/CeO_2, respectively. Note the nearly constant Fe^{3+} fraction for the $Fe(NO_3)_3$-derived material.

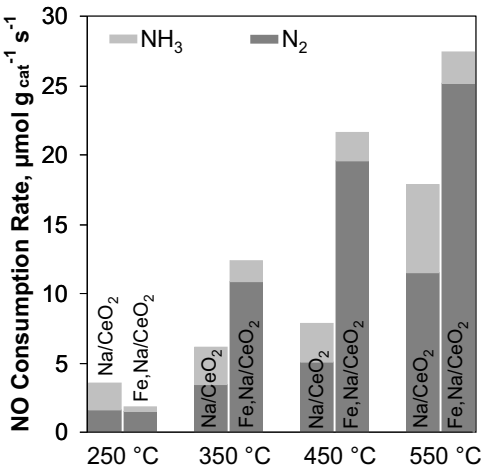

Fig. 7. Rates of NO consumption toward NH_3 and N_2 for Na/CeO_2 (0.5 Na nm^{-2}) and FeO_x–Na/CeO_2 derived from NaFeEDTA on CeO_2 (0.6 Fe nm^{-2}) at different temperatures. Differences in activity between support and catalysts are greatest at 450 °C. Fe-containing materials are more selective toward reduction of NO to N_2 relative to the support.

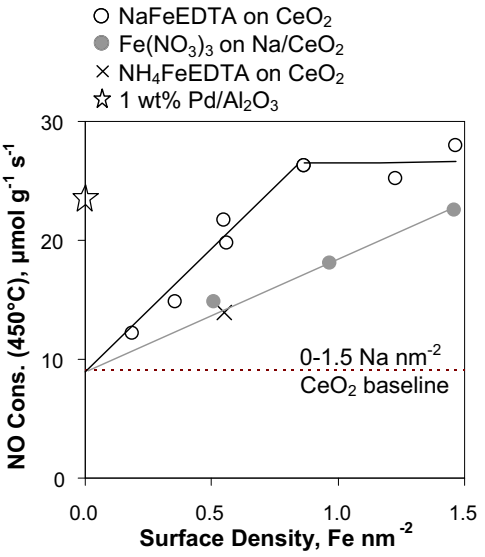

Fig. 8. Total consumption rate of NO vs. surface density for FeO_x–Na/CeO_2 prepared from NaFeEDTA on CeO_2 and $Fe(NO_3)_3$ on Na/CeO_2. Dashed line marks the baseline activity of Na/CeO_2. Catalyst performance is compared to that of Na-free catalyst (NH_4FeEDTA on CeO_2, *X*) and a reference 1 wt% Pd/Al_2O_3 catalyst (*, on *Y*-axis).

NaFeEDTA on CeO_2 produces a larger fraction of reducible Fe species than $Fe(NO_3)_3$ on Na-modified CeO_2. This is made clear in Fig. 6, which shows the Fe^{3+} fraction determined by XANES as function of temperature for two materials with similar surface densities but different precursors: 0.9 Fe nm^{-2} prepared from NaFeEDTA on CeO_2 and 1.0 Fe nm^{-2} prepared from $Fe(NO_3)_3$ on Na/CeO_2.

Recalling that the starting Fe oxidation state was always less than 3+, the presence of Fe^{2+} even before reduction suggests that a fraction of the CeO_2 was initially present as Ce(III) and reduced Fe^{3+} to Fe^{2+} during the initial synthesis. The density of permanently reduced Fe^{2+} species remains in the narrow range of 0.11 ± 0.02 Fe nm^{-2} for all materials prepared from NaFeEDTA and 0.16 Fe nm^{-2} for those derived from $Fe(NO_3)_3$.

Combining the TPR and XANES data generates a picture of the FeO_x speciation from the two precursors. Taking 0.6 Fe nm^{-2} as an example, the EDTA precursor leads to ~0.1 Fe nm^{-2} as permanently reduced Fe^{2+}, ~0.3 Fe nm^{-2} of Fe^{3+} species reducible at ~400 °C, and ~0.2 Fe nm^{-2} as any one of a number of redox-inactive Fe^{3+} species. The nitrate precursor, in contrast, leads to fewer of the redox-active sites (~0.15 Fe nm^{-2}), and more of the permanently reduced and unreducible sites (~0.15 and ~0.3 Fe nm^{-2}, respectively).

3.7. Catalytic reduction of NO by H_2

FeO_x–CeO_2 and FeO_x–Na/CeO_2 materials were tested as catalysts in the reduction of NO by stoichiometric H_2 between 150 °C and 550 °C. NO conversions range from 14% to 63%, with values increasing monotonically with temperature and Fe loading, as expected. Direct decomposition of NO in the absence of H_2 over the oxidized materials is not observed in this temperature range. Using only N_2 and NH_3 as products, the N balance – defined as moles of N in products over moles of consumed NO – is between 75% and 105% for 350 °C and above. The lower values are observed at lower temperatures and conversions, and the discrepancy is attributed to limits in instrumental precision.

Fig. 7 shows the rate of consumption of NO, in μmol g_{cat}^{-1} s^{-1}, of a representative catalyst (0.6 Fe nm^{-2} from NaFeEDTA on CeO_2) and a related Na-modified support (0.5 Na nm^{-2} on CeO_2) at four different temperatures. Na/CeO_2 and CeO_2 display moderate baseline activity that is largely independent of alkali loading. Supports show selectivity toward N_2 between 45 and 65% while Fe-containing materials are 85–95% selective toward N_2. Interestingly, Fe-containing materials do not exceed the baseline activity of the support below 350 °C. Recall that 350 °C marks the onset of reduction of Fe species capable of Fe^{3+}–Fe^{2+} cycles. This suggests a relation between those Fe surface structures and activity of these FeO_x–CeO_2 materials in NO reduction.

Fe-containing materials show the greatest difference relative to the support at 450 °C (Fig. 7). Hence, reaction rates at that temperature will be used when discussing the effects of Fe surface density and precursor.

3.7.1. Catalyst preparation vs. activity

First, catalysts were tested for the role of the Na promoter. At a representative surface density of 0.5 Fe nm^{-2} and 450 °C, NaFeEDTA/CeO_2 outperforms NH_4FeEDTA/CeO_2 (material 8, Table 1, no alkali) by >40% (Fig. 8). Considering that Na has no effect on the background rate of reaction by the support, Na promotion nearly doubles the Fe-associated contribution to the NO reduction rate. Different methods of addition for Na and $FeEDTA^-$ (NaFeEDTA on CeO_2 vs. NH_4FeEDTA on Na/CeO_2, e.g. material 9 in Table 1) give identical rates within uncertainty. For all loadings, the NaFeEDTA precursor is seen to outperform the nitrate precursor, but particularly at lower loadings. From these comparisons, both the chelating ligand and the alkali dopant are necessary for the highest performance. Beyond these internal comparisons, the reduction of NO with H_2 at 450 °C by these FeO_x–Na/CeO_2 materials compares favorably to that of a Pd/Al_2O_3 standard (Fig. 8): 1.0 wt% FeO_x–CeO_2 from NaFeEDTA shows a rate of 26 μmol (g cat)$^{-1}$ s^{-1}, while 1.0 Pd wt% Pd/Al_2O_3 shows a rate of 24 μmol (g cat)$^{-1}$ s^{-1}.

Finally, for heat-treated materials prepared from NaFeEDTA on CeO_2, the integrated NO consumption rate at 450 °C increases linearly with Fe content up to 0.9 Fe nm^{-2}, where it enters a plateau in activity (Fig. 8). If one recalls, 0.9 Fe nm^{-2} also marks the onset of a plateau in the surface density of species capable of Fe^{3+}–Fe^{2+} redox cycling (Fig. 4). Based on the common trend, the activity of these materials is assigned to redox-cycling Fe species. A similar assignment can be made for materials prepared from $Fe(NO_3)_3$ on Na/CeO_2, but the relation here is simpler because the population of redox-active Fe and absolute NO reduction rate are both linear with respect to Fe loading.

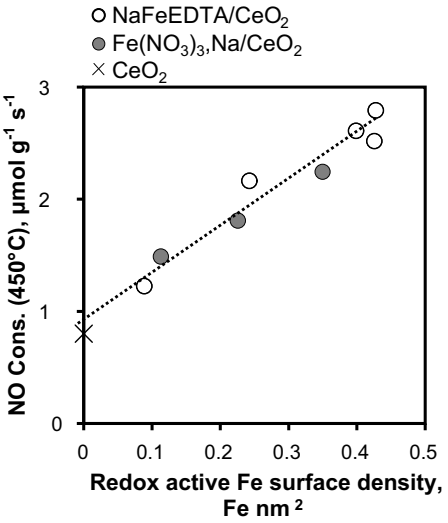

Fig. 9. Parametric plot of integrated NO reduction rate with H_2 (450 °C), against amount of redox-cycling FeO_x in a given catalyst sample. A single trendline is seen including FeO_x–Na/CeO_2 prepared from both NaFeEDTA on CeO_2 and $Fe(NO_3)_3$ on Na/CeO_2.

Fig. 9 plots the observed integrated rates for all the FeO_x–Na/CeO_2 materials, regardless of precursor, against the number of redox-cycling Fe. While the rate data were not acquired under differential conditions, these rates are independent of P_{H2} and P_{NO} between 0.01 and 0.03 atm (Supporting Information Fig. S5), covering the range of conversions (14–63%) exhibited by these catalysts. In Fig. 9, all materials collapse to a single trendline. Materials derived from $Fe(NO_3)_3$ give lower levels of redox-active Fe and correspondingly lower rates. The plateau in both redox-active Fe and NO reduction rate for NaFeEDTA-derived materials is seen as a cluster of points at the upper end of the plot. The single trendline for different redox-capable Fe populations, present in different surface densities and prepared by different methods, supports their assignment as the active phase.

4. Conclusions

This work illustrates a straightforward methodology to create materials for the reduction of NO to N_2 with H_2 based on Fe oxides loaded on CeO_2 instead of precious metals. Akali cations, added before or simultaneously to the Fe precursor, appear to serve as structural promoters, increasing observed rates beyond that of FeO_x–CeO_2 alone. Although the exact role of the promoter remains under investigation, it may act by titrating the surface vacancies that would otherwise incorporate Fe cations and form inactive species. These materials containing under-coordinated Fe surface structures on Na/CeO_2 show NO reduction rates, per mass of catalyst, comparable to those of similar loadings of Pd on Al_2O_3. The activity of these materials in the reduction of NO with H_2 is correlated to a subset of the FeO_x oligomers present on the surface, as determined from DRUV–vis, TPR, and XANES. These active structures are capable of undergoing reversible Fe^{3+}–Fe^{2+} redox cycles under reaction conditions, as demonstrated from repeated TPR cycles.

These redox-active surface structures are most selectively formed by incipient wetness impregnation of CeO_2 with aqueous NaFeEDTA – a bulky, negatively charged complex. The EDTA ligand gives more of the redox-active FeO_x and less of the permanently reduced and the redox-inactive FeO_x species, as compared to a more typical $Fe(NO_3)_3$ precursor. For all materials prepared from NaFeEDTA on CeO_2 and $Fe(NO_3)_3$ on Na/CeO_2, rates collapse to a single trendline when plotted against the amount of FeO_x undergoing reversible Fe^{3+}–Fe^{2+} cycles. This correlation, in spite of the difference in precursor, supports the hypothesis that this particular sub-population of surface structures is responsible of the activity of these materials. The identity of these FeO_x sites is currently under scrutiny by other techniques. More rigorous kinetic evaluation with reductants more relevant to real tailpipe emissions (e.g. CO and hydrocarbons) is also underway and will be reported elsewhere. Finally, further optimization of the promoter type, promoter amount, and the Fe precursor identity offers opportunities for additional enhancement of catalytic reactivity.

Acknowledgements

J.M.N. and D.P.C. acknowledge the support of Toyota Motor Company and thank Pria Young and Boone Thompson for helpful discussions. Portions of this work were performed with the invaluable help of Dr. Qing Ma at the DuPont–Northwestern–Dow Collaborative Access Team (DND-CAT) located at Sector 5 of the Advanced Photon Source (APS). DND-CAT is supported by E.I. DuPont de Nemours & Co., The Dow Chemical Company, and Northwestern University. Use of APS, an Office of Science User Facility operated for the U.S. Department of Energy (DOE) Office of Science by Argonne National Laboratory, was supported by the U.S. DOE under contract no. DE-AC02-06CH11357. JMN and TRE acknowledge theDOE Office of Basic Sciences grant SC-0006718, which supported materials characterization activities.

Appendix A. Supplementary data

Supplementary data associated with this article can be found, in the online version, at http://dx.doi.org/10.1016/j.apcatb.2014.11.055.

References

[1] J. Kašpar, P. Fornasiero, N. Hickey, Catal. Today 77 (2003) 419–449.
[2] B.J. Adelman, T. Beutel, G.D. Lei, W.M.H. Sachtler, J. Catal. 158 (1996) 327–335.
[3] C. Chupin, A.C. van Veen, M. Konduru, J. Després, C. Mirodatos, J. Catal. 241 (2006) 103–114.
[4] M. Schwidder, M.S. Kumar, K. Klementiev, M.M. Pohl, A. Brückner, W. Grünert, J. Catal. 231 (2005) 314–330.
[5] S. Brandenberger, O. Kröcher, A. Wokaun, A. Tissler, R. Althoff, J. Catal. 268 (2009) 297–306.
[6] S. Brandenberger, O. Kröcher, A. Tissler, R. Althoff, Appl. Catal. B: Environ. 95 (2010) 348–357.
[7] M. Santhosh Kumar, M. Schwidder, W. Grunert, A. Bruckner, J. Catal. 227 (2004) 384–397.
[8] F. Heinrich, C. Schmidt, E. Löffler, M. Menzel, W. Grünert, J. Catal. 212 (2002) 157–172.
[9] R. Joyner, M. Stockenhuber, J. Phys. Chem. B 103 (1999) 5963–5976.
[10] H.-Y. Chen, W.M.H. Sachtler, Catal. Today 42 (1998) 73–83.
[11] H. Xia, K. Sun, Z. Liu, Z. Feng, P. Ying, C. Li, J. Catal. 270 (2010) 103–109.
[12] J. Valyon, W.S. Millman, W.K. Hall, Catal. Lett. 24 (1994) 215–225.
[13] S.-H. Choi, B.R. Wood, J.A. Ryder, A.T. Bell, J. Phys. Chem. B 107 (2003) 11843–11851.
[14] Z.-X. Gao, H.-S. Kim, Q. Sun, P.C. Stair, W.M.H. Sachtler, J. Phys. Chem. B 105 (2001) 6186–6190.
[15] A.S. Reddy, C.-Y. Chen, C.-C. Chen, S.-H. Chien, C.-J. Lin, K.-H. Lin, C.-L. Chen, S.-C. Chang, J. Mol. Catal. A: Chem. 318 (2010) 60–67.
[16] K. Chen, L. Dong, Q. Yan, Y. Chen, J. Chem. Soc., Faraday Trans. 93 (1997) 2203–2206.
[17] N. Apostolescu, B. Geiger, K. Hizbullah, M.T. Jan, S. Kureti, D. Reichert, F. Schott, W. Weisweiler, Appl. Catal. B: Environ. 62 (2006) 104–114.
[18] A. Parmaliana, F. Arena, F. Frusteri, A. Marinez-Arias, M.L. Granados, J.L. Fierro, Appl. Catal. A 226 (2002) 163–174.
[19] M. Stockenhuber, R.W. Joyner, J.M. Dixon, M.J. Hudson, G. Grubert, Microporous Mesoporous Mater. 44–45 (2001) 367–375.
[20] F. Arena, G. Gatti, S. Coluccia, G. Martra, A. Parmaliana, Catal. Today 91–92 (2004) 305–309.
[21] F. Arena, G. Gatti, G. Martra, S. Coluccia, L. Stievano, L. Spadaro, P. Famulari, A. Parmaliana, J. Catal. 231 (2005) 365–380.
[22] J.D. Henao, B. Wen, W.M.H. Sachtler, J. Phys. Chem. B 109 (2004) 2055–2063.
[23] A.W. Holland, G. Li, A.M. Shahin, G.J. Long, A.T. Bell, T.D. Tilley, J. Catal. 235 (2005) 150–163.

[24] C. Nozaki, C.G. Lugmair, A.T. Bell, T.D. Tilley, J. Am. Ceram. Soc. 124 (2002) 13194–13203.
[25] A. Badri, C. Binet, J.-C. Lavalley, J. Chem. Soc., Faraday Trans. 92 (1996) 4669–4673.
[26] S. Bernal, J.J. Calvino, G.A. Cifredo, J.M. Gatica, J.A.P. Omil, J.M. Pintado, J. Chem. Soc., Faraday Trans. 89 (1993) 3499–3505.
[27] D. Prieto-Centurion, A.M. Boston, J.M. Notestein, J. Catal. 296 (2012) 77–85.
[28] D. Prieto-Centurion, J.M. Notestein, J. Catal. 279 (2011) 103–110.
[29] S. Brunauer, P.H. Emmett, E. Teller, J. Am. Chem. Soc. 60 (1938) 309–319.
[30] P. Kubelka, F. Munk, Z. Tech. Phys. 12 (1931) 593–601.
[31] R. Meier, F.W. Heinemann, Inorg. Chim. Acta 337 (2002) 317–327.
[32] G. McLendon, R.J. Motekaitis, A.E. Martell, Inorg. Chem. 15 (1976) 2306–2308.
[33] S. Bordiga, R. Buzzoni, F. Geobaldo, C. Lamberti, E. Giamello, A. Zecchina, G. Leofanti, G. Petrini, G. Tozzola, G. Vlaic, J. Catal. 158 (1996) 486–501.
[34] F. Arena, F. Frusteri, L. Spadaro, A. Venuto, A. Parmaliana, Stud. Surf. Sci. Catal. 143 (2000) 1097–1105.
[35] L. Dong, Y. Chen, J. Chem. Soc., Faraday Trans. 92 (1996) 4589–4593.
[36] M. Wilke, F. Farges, P.-E. Petit, G.E. Brown, F. Martin, Am. Mineral. 86 (2001) 714–730.